Application of hyperbolic stress–strain models for sandstone and shale to fold wavelength in the Mexican Ridges foldbelt

THOMAS M. THARP and M. GINGER SCARBROUGH

Department of Earth and Atmospheric Sciences, Purdue University, West Lafayette, IN 47907, U.S.A.

Abstract—The Mexican Ridges foldbelt on the continental slope east of Mexico has major folds with wavelengths averaging 7 km. Locally, there are also small amplitude, near-surface folds with wavelengths of 2 km. Initial dominant wavelength is modelled by the finite element method using the hyperbolic stress–strain relationship originally derived for soils. Hyperbolic stress–strain models for sandstone and shale are calibrated using field porosity–depth relationships for shale, and laboratory one-dimensional consolidation data for sand and clay. Effective tangent Young's modulus calculated from hyperbolic stress–strain models is generally higher for sandstones than for shales, and for both rock types modulus increases substantially with depth.

The finite element models of dominant wavelength duplicate the two orders of folds observed in the Mexican Ridges and match their wavelengths. In the models, fold wavelength is nearly constant for large variations in both sandstone fraction in the folded section and pore pressure magnitude in the overpressured basal shale below the folded section, but fold amplification is increased by high pore pressure in the basal shale and by high sandstone fraction in the folded section. Fold wavelength is affected more by depth distribution of high pore pressure than by pressure magnitude, and on the lower continental slope where grain size may be smaller, a thicker zone of high pressure would partly explain the modest downslope increase in fold wavelength.

INTRODUCTION

THE Mexican Ridges foldbelt, located in the western Gulf of Mexico, extends nearly 400 km along the continental slope (Fig. 1). Our study area is a small part of that belt defined by the four seismic sections (Buffler *et al.* 1979) shown in Fig. 1. In the study area, folds have topographic relief of up to 150 m and wavelengths for larger folds are 3–14 km. The general seismic stratigraphy of the Mexican Ridges province was developed by Buffler *et al.* (1979) and is shown in Table 1. Scarbrough
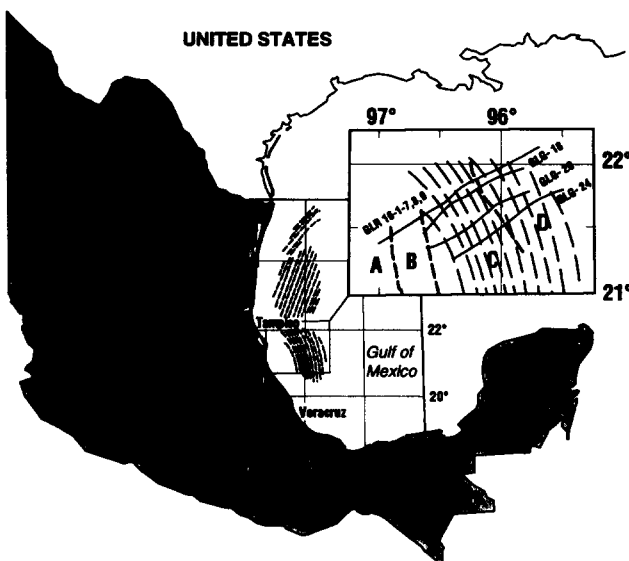

Fig. 1. Location of Mexican Ridges foldbelt. Dashed curves are schematic representations of fold trends (after Bryant *et al.* 1968). Solid curves are seismic lines and heavy dashed lines of the insert delineate structural domains (after Buffler *et al.* 1979).

(1992) has further differentiated the stratigraphy of the study area based on seismic signature, correlations with DSDP holes in the deep Gulf of Mexico and sedimentation in adjacent coastal basins.

Structural features of the Mexican Ridges foldbelt

Buffler *et al.* (1970) distinguished four deformational zones across the foldbelt (Fig. 2). Zone A nearest the Mexican Coast is characterized by growth faults and shallow slumps. Farther east, zone B consists of a thick sedimentary sequence ponded behind the first high-amplitude fold. Zone C encompasses the area of high-to-medium-amplitude folds that constitute the main part of the foldbelt. In zone D fold amplitudes decrease seaward.

Individual fold axes plunge and die out or change amplitude and overall character along strike (Buffler *et al.* 1979), but some fold axes have been traced for over 60 nautical miles (Bryant *et al.* 1968). In zones C and D, second-order folds occur locally in shallow units (latest Miocene to Holocene). In Fig. 2, three such folds are observed on the crest of a first-order anticline with its top at a sea floor depth equivalent to three seconds two-way travel time. In the study area, the shallow second-order folds have wavelengths of approximately 2 km, and are superimposed on the larger, first-order folds which have wavelengths loosely clustered about 7 km (Fig. 3). All folding seems to be restricted to the upper seismic units (Sigsbee-Cinco de Mayo and Upper Mexican Ridges).

Most seismic sections show several imbricate landward-dipping thrust faults (Buffler *et al.* 1979, Pew 1982). The faults are thought to flatten with depth and die out in the reflectionless lower Mexican Ridges and

Table 1. Generalized seismic units of the Mexican Ridges Province (modified from Buffler *et al.* 1979, reprinted by permission)

Unit	Age	Seismic characteristics	Inferred lithology
Sigsbee-Cinco de Mayo	Late Miocene to Holocene	Strong, discontinuous reflectors. Prominent zone of large-scale cross-beds in middle of unit	Alternating hemipelagic silty clays, fine-grained thin turbidites and sandy turbidites
Mexican Ridges	Early Tertiary (?) to Mid-Miocene	Strong, discontinuous reflectors in upper part; reflectionless zone in lower part. Lower boundary is sequence of strong, discontinuous reflections	Mostly sandy turbidites in upper part, fine-grained turbidites and hemipelagic sediments in lower part. Possible sandy turbidites at base
Campeche	Mid-Cretaceous (?) to Early Tertiary (?)	Generally weak reflectors to transparent. Strong, discontinuous reflections near bottom	Mostly fine-grained, homogeneous pelagic or hemipelagic sediments. Possible turbidites toward base
Challenger	Jurassic (?) to Mid-Cretaceous (?)	Upper part is sequence of strong reflections	Possible deep water carbonates

upper Campeche units. The growth faults on the landward side of the folds (Buffler *et al.* 1979, Pew 1982) shallow with depth and become untraceable in the deep reflectionless zone. Folding is thought to be accommodated by flow in the basal overpressured shale (Buffler *et al.* 1979). The shale is soft enough to rise diapirically into anticlines of the Mexican Ridges south of the study area, where the folds have been buried by sediments.

Buffler (1991) assigns the initiation of folding in the Mexican Ridges to Oligocene–Miocene time. Pew (1982) suggests a Middle Miocene age for fold initiation just south of the study area, with fold initiation in Late Pliocene or Early Pleistocene in zone D of the study area. The folds restricted sediment influx to the Veracruz Tongue on the east by early Late Miocene (Bertagne 1984) and they remain active to the present.

Cause of folding

Early investigations (Jones *et al.* 1967, Bryant *et al.* 1968, Emery & Uchupi 1972, Massengill *et al.* 1973) developed several hypotheses but generally interpreted the folding to be the result of salt diapirism. With the realization that the folds are not salt cored, Buffler *et al.* (1979) proposed that folding results from gravity sliding or from compression related to subduction beneath the Middle America trench, transmitted to the Mexican Ridges Province through deep-seated foreland thrusts. Both mechanisms allow for detachment along a décollement within the lower Mexican Ridges and upper Campeche units.

Several lines of evidence favor the gravity sliding hypothesis. Garrison & Martin (1973) point out that along strike the foldbelt is composed of two lobes, each convex downslope, as would be expected with gravity sliding. Pew (1982) argues against foreland thrusting as a mechanism for folding. He notes that fold axes reflect the trend of the continental margin rather than the subduction zone. Also, foreland thrusting should have affected the thick Tertiary basins within the Gulf Coastal Plain. These basins have undergone extensive growth faulting, but show little sign of the compression expected in a foreland thrusting model. Suter (1987) concluded from borehole stress indicators to depths of 4912 m that

the east coast of Mexico is under E–W to SE–NW extension, suggesting that active deformation in the Mexican Ridges foldbelt is not caused by external horizontal compression. Current interpretation generally favors the gravity sliding hypothesis (Ewing 1991, Bryant *et al.* 1991, Buffler 1991).

If folding is gravity driven it is possible that this unusual occurrence of prominent, wide-spread folding results from an atypical slope profile. Most continental slopes have a large, steep drop at the shelf-slope break with a gentle lower slope. Instability is manifested by listric normal faults. Because the Mexican Ridges slope exhibits little drop at the shelf-slope break, its downslope continuation is a broad zone of moderate and relatively constant slope. Flattening at the base of the slope provides the end constraint necessary for a broad upslope zone of compression. The moderate slope angle also allowed accumulation of sandy turbidites that might have bypassed a steeper slope. Similar folding might have occurred on the northern slope of the Gulf of Mexico except that incompetent salt extending all the way to abyssal depths allows easy deformation at the toe of the slope in the Sigsbee escarpment. Only on the east and west ends of the northern slope is the toe sufficiently buttressed to allow the folding of the Mississippi Fan and Perdido foldbelts.

Rheology

For highly stressed, fault-dominated sedimentary rocks such as those of accretionary wedges or growth faults, high strains lead to general failure that is well characterized by Mohr–Coulomb plasticity (Westbrook & Smith 1983, Davis *et al.* 1983, Xiao *et al.* 1991). Less is known of the rheology of more weakly deformed young sedimentary rocks, like those of the Mexican Ridges, in which gentle folds, diapirs, and compaction structures form largely by deformation as a continuum. Substantial inelastic deformation may occur in this environment with little faulting, and neither linear elastic nor Mohr–Coulomb plastic models represent such rocks adequately for quantitatively accurate modelling.

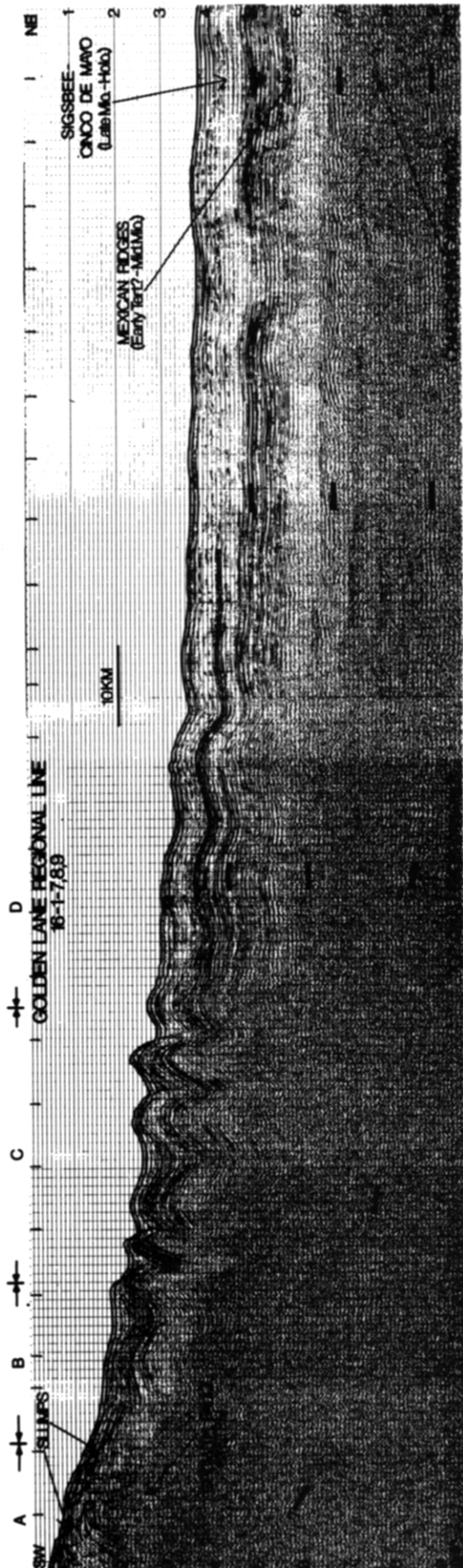In young sedimentary rocks, compaction is the most important inelastic deformation in the absence of

Fig. 2. Profile GLR 16-1-7, 8, 9 showing general seismic units and deformational zones (from Buffler *et al.* 1979, reprinted by permission).
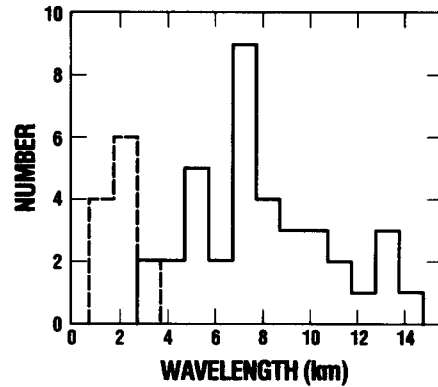

Fig. 3. Histogram of fold wavelengths in the four seismic sections. The dashed line refers to shallow second-order folds, the solid line to first-order folds.

nism. In many basins, compaction results in known porosity–depth relationships that can be used to calibrate rheologic models. It is therefore useful to evaluate the mechanisms of compaction in sandstone and shale and the conditions under which different types of rheologic models may be valid.

Compaction of sandstone

Field evidence suggests that simple mechanical compaction of sandstone is important near the surface, but at depth it is commonly arrested by cementation or supplanted by pressure solution. Mechanical compaction is considered significant to depths of 1.2 km in the Texas Gulf Coast (Loucks *et al.* 1979, 1984, Loucks & Dodge 1980) and to depths of 1–1.5 km for a suite of Tertiary sandstones in Germany (Fuchtbauer 1967). However, some sands are observed to remain uncemented and hence subject to mechanical compaction to greater depths. For example, the rapidly deposited Pliocene turbidite sandstones of the Ventura anticline have remained virtually uncemented at depths of 4.6–6.1 km (Hsu 1977). Stanton (1977) notes that sandstones with high matrix content experience slower cementation, and hence greater mechanical compaction than clean sands.

Pressure solution can significantly influence compaction and other deformation in sandstones, but its role is uncertain. Tada & Siever (1989) note that most documented pressure solution is in pre-Tertiary rocks. They observe also that it can be prevented by cementation. Perhaps for those reasons it is limited in Tertiary rocks of the U.S. Gulf Coast (Land 1984), a geologic environment somewhat similar to the Mexican Ridges. However, where conditions are favorable, pressure solution may be important at depths greater than 1–1.5 km (Tada & Siever 1989, Gratz 1991). At depths in excess of 3 km large pressure solution strains occur locally (Houseknecht 1988).

Compaction of shale

Argillaceous sediments compact in a primary compression stage by progressive reorientation and re-

arrangement of grains with fluid expulsion (e.g. Rieke & Chilingarian 1974, pp. 1–27, Magara 1978, pp. 11–36, Sowers 1979, pp. 148–176, Oertel 1983). In laboratory consolidation tests this stage ends when excess pore pressures become zero. A more gradual secondary compression follows, resulting from plastic deformation and failure of grains (Sowers 1979, pp. 148–176) and possibly re-equilibration of tightly bound water (Ladd et al. 1977). These mechanical compaction processes produce large strains in response to increased load, and where permeability of adjacent units prevents overpressuring, strain in response to new loads is rapid enough that time dependence is insignificant in modelling slow processes such as folding.

POROSITY–DEPTH RELATIONSHIPS

To calibrate a rheologic model, both stresses and strains must be known. The best hope for constraining these parameters lies in data from young sedimentary basins which have undergone relatively uninterrupted sedimentation and have no history of horizontal compression. Porosity–depth curves for sandstone and shale from these basins serve as indirect indicators of the vertical strains associated with compaction. One-dimensional consolidation tests performed in the laboratory are mechanically analogous to compaction deformation, and are also used to calibrate hyperbolic stress–strain models (described below) for sandstone and shale.

Field porosity–depth relationships suggest that porosity (as well as compaction) of deeply buried sandstones may be primarily controlled by cementation and/or pressure solution. Porosity–depth curves for normally consolidated Cenozoic sandstones are shown as solid lines in Fig. 4. The term 'normally consolidated' indicates that present depth is approximately equal to maximum burial depth. Laboratory data for unconsolidated, uncemented sands compacted in one-dimensional consolidation tests (horizontal strain = zero) are shown as

dashed lines. For laboratory data, equivalent depths are computed from effective compaction stress (stress minus pore pressure) using Eaton's (1969) vertical stress gradient and a normal hydrostatic pore pressure gradient of 0.0105 Mpa m^{-1} (Loucks et al. 1981). At low vertical stress (depths to 1 km), porosities may be similar for the two data sets. At greater vertical stress, porosities decrease more gradually with depth for laboratory compacted sands than for natural sandstones. Similarity between field and laboratory data at shallow depth suggests that grain re-arrangement and fracture may be dominant to a depth of at least 1 km.

Well-cemented sandstones can probably be approximated as linear elastic. Deformation of uncemented sandstones probably resembles that observed experimentally for sands, at least at shallow depth, and perhaps deeper where conditions (as yet poorly understood) do not favor pressure solution. Sandstones not strongly affected by cementation or pressure solution are best characterized by an inelastic rheology when normally consolidated, although their behavior, like that of soils, should be nearly linear elastic during unloading (Karig & Hou 1992). Figure 5 shows porosity–depth curves for experimentally deformed sands only. The solid curves, drawn by hand for high, low and intermediate porosities are used to calibrate hyperbolic stress–strain models.

Porosity–depth curves for normally consolidated Cenozoic clays and shales are shown in Fig. 6. Porosities may be anomalously high in some curves because of high pore pressures. However, if the natural clays and shales plotted here follow the trend for the U.S. Gulf Coast, large anomalous pore pressures would be expected below 2.5–3 km. At such depths, they would have little effect on the curves in Fig. 6. Data for laboratory one-dimensional consolidation of clays are shown in Fig. 7. For these data, drained loading and secondary compression was achieved by maintaining a given applied load until the strain rate approaches zero; at that point, an additional load increment is applied. Figure 8 shows the
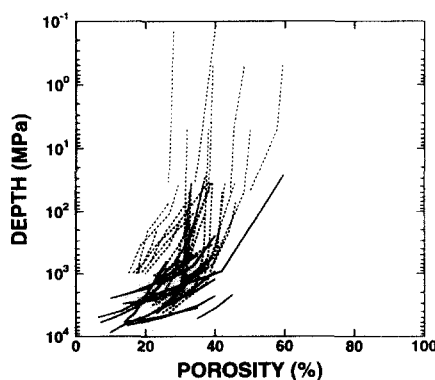

Fig. 4. Porosity vs depth for field sandstones (solid) and laboratory sands (dashed). Field sandstone data from: Maxwell (1964), Galloway (1974), Scholle (1977), Selley (1978), Sclater & Christie (1980), and Loucks et al. (1984). Laboratory sand data from: Gilboy (1928), Roberts & De Souza (1958), van der Knapp & van der Vlis (1967), Allen & Mayuga (1969), Roberts (1969), Sawabini et al. (1974), Allen & Chilingarian (1975), Karig & Hou (1992).
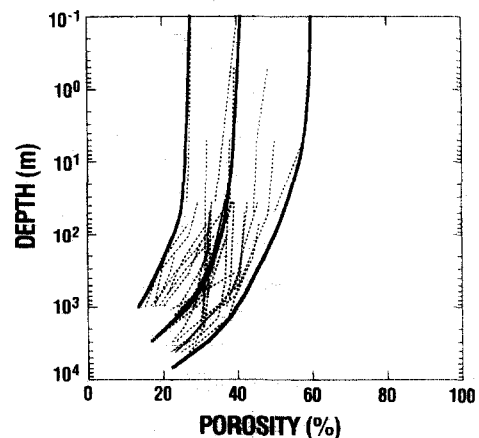

Fig. 5. Porosity vs equivalent depth for sands tested in the laboratory under one-dimensional consolidation, also shown in Fig. 4. Solid curves, representing low, intermediate and high porosity, are the curves for which hyperbolic stress–strain parameters are calculated. See Fig. 4 for sources of data.
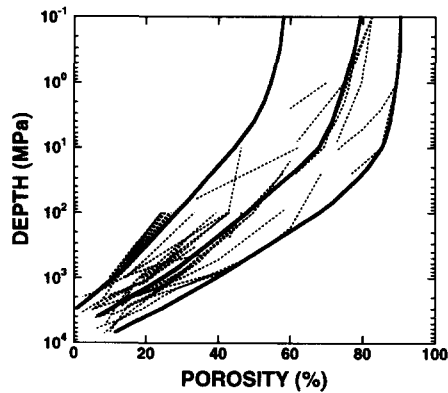
Fig. 6. Porosity vs depth for field shales and clays. Solid curves, representing low, intermediate and high porosity, are the curves for which hyperbolic stress–strain parameters are calculated. Data from: Hedberg (1936), Emery & Rittenberg (1952), Dickson (1953), Kidwell & Hunt (1958), Gould (1960), Richards & Keller (1962), Meade (1963), Philipp et al. (1963), Foster & Whalen (1966), Boatman (1967), Rochon (1967), Magara (1968, 1978, pp. 11–85, 119–142), Brown (1969), Griffin & Bazer (1969), Heting (1969), Bouma et al. (1972), Dickey (1972), Reike & Chilingarian (1974, p. 42), Wolf & Chilingarian (1976), Tompkins & Shephard (1979), Nobes (1986), Nobes et al. (1986).
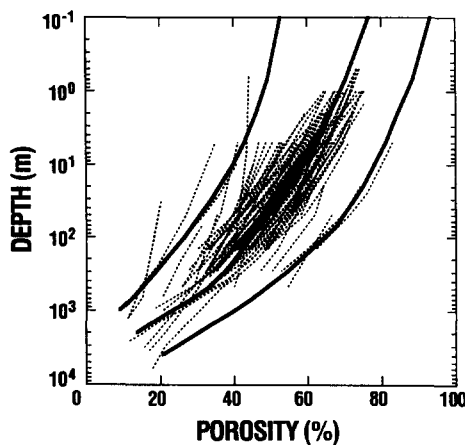

Fig. 7. Porosity vs equivalent depth for clays tested under one-dimensional consolidation. Solid curves, representing low, intermediate and high porosity, are the curves for which hyperbolic stress–strain parameters are calculated. Data from: Skempton (1944, 1953), Chilingarian & Knight (1960), Bryant et al. (1967, 1974, 1975), van der Knapp & van der Vlis (1967), Allen & Mayuga (1969), Keller & Bennett (1973), Allen & Chilingarian (1975), Kharaka & Berry (1976), Karig & Hou (1992).
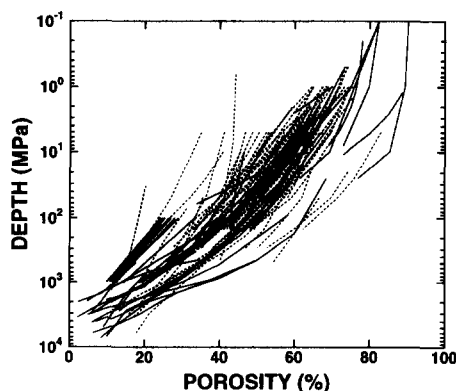

Fig. 8. Porosity vs depth for field shales and clays (solid) and laboratory clays (dashed) of Figs. 6 and 7.

field and laboratory data plotted together. The data sets generally overlap and exhibit similar trends. This would be expected if compaction mechanisms observed in the laboratory also govern deformation in the field.

HYPERBOLIC STRESS–STRAIN MODEL

Shales and uncemented sandstones in young sedimentary basins exhibit compaction behavior much like that of sands and clays compacted in the laboratory. Several soil mechanics models represent the large strains that occur above the elastic limit but below the Mohr–Coulomb failure envelope (see Yong & Ko 1981). These models are successful in civil engineering practice, but few have been applied to geological settings (Kosloff et al. 1980, Jones & Addis 1986). The model chosen for this study is the hyperbolic stress–strain law. It was selected because: (1) it is based on sufficiently fundamental principles that it successfully models both sand and clay; (2) it does not require empirical constants that must be obtained through extensive laboratory tests; (3) its parameters are physically meaningful and some can be evaluated independently. Deformation in the Mexican Ridges foldbelt is unusually well suited to modelling by the hyperbolic stress–strain models derived for young sedimentary basins. With modest strains and minor faulting, folding has proceeded largely by continuum deformation. Because it has remained continuously below sea level, no erosion or overconsolidation (by reduction of vertical stress) (Das 1983, pp. 253–338) has occurred. This relative structural and stratigraphic simplicity has largely held the foldbelt within the restrictive mechanical conditions to which our hyperbolic stress–strain models apply. Details of the hyperbolic stress–strain model and its application in numerical stress analysis are discussed by Duncan & Chang (1970), Duncan (1981), and Vaid (1985).

The governing equation:

$$\sigma_1 - \sigma_3 = \frac{\varepsilon}{\dfrac{1}{E_i} + \dfrac{\varepsilon}{(\sigma_1 - \sigma_3)_{ult}}} \tag{1}$$

is derived from the assumption that the relationship between stress and strain is hyperbolic. Stresses σ_1 and σ_3 are maximum and minimum effective principal stresses, respectively (where compression is considered positive and effective stress is normal stress minus pore pressure), ε is strain in the σ_1 direction, E_i is the effective Young's modulus for $\sigma_1 = \sigma_3$ and $(\sigma_1 - \sigma_3)_{ult}$ is the asymptotic value of the stress difference for infinite ε. The parameters are illustrated in Fig. 9. E_i is assumed to vary with effective confining pressure σ_3 as

$$E_i = k p_a \left(\frac{\sigma_3}{p_a}\right)^n \tag{2}$$

(Jaky 1944), where k and n are empirically determined material constants; p_a, atmospheric pressure, is introduced to make k and n dimensionless. The asymptotic
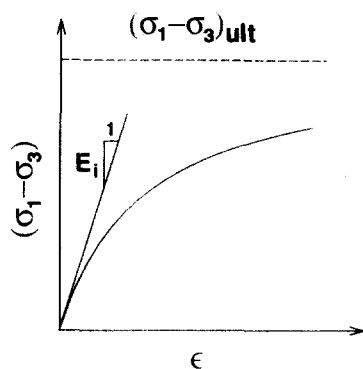
Fig. 9. Hyperbolic stress–strain relationship.

stress difference $(\sigma_1 - \sigma_3)_{ult}$ can be stated in terms of the Mohr–Coulomb failure stress $(\sigma_1 - \sigma_3)_f$ as

$$(\sigma_1 - \sigma_3)_{ult} = \frac{1}{R_f}(\sigma_1 - \sigma_3)_f. \tag{3}$$

where R_f is an empirical constant less than 1.0 that lies between 0.5 and 0.9 for most soils (Duncan & Chang 1970). Stating $(\sigma_1 - \sigma_3)_f$ in terms of σ_3 yields

$$(\sigma_1 - \sigma_3)_{ult} = \frac{1}{R_f}\left(\frac{2c \cos\phi + 2\sigma_3 \sin\phi}{1 - \sin\phi}\right), \tag{4}$$

where c and ϕ are cohesion and friction angle of the soil. For incremental loading analysis, the effective tangent Young's modulus E_t can be written

$$E_t = \left(1 - \frac{R_f(1 - \sin\phi)(\sigma_1 - \sigma_3)}{2c \cos\phi + 2\sigma_3 \sin\phi}\right)kp_a\left(\frac{\sigma_3}{p_a}\right)^n. \tag{5}$$

Application of the equation to general problems of two- and three-dimensional incremental elasticity, such as those considered here, requires a second constant. Effective Poisson's ratio, ν (Duncan & Chang 1970), is used in this analysis, although bulk modulus would be equally valid (Duncan 1981). Because loading is monotonic in this study, effective stiffness for unloading and reloading (Duncan 1981) is not addressed.

EVALUATION OF PARAMETERS FOR THE HYPERBOLIC STRESS–STRAIN MODEL

Each curve in Figs. 5–7 represents a unique material and a unique stress–strain history. Best-fitting parameters for the hyperbolic stress–strain model might be found for each curve, however, most curves record porosity variation for only a small range of stress. Such short curves, taken alone, would not sufficiently constrain a model over the large stress/depth range important in Mexican Ridges and other geologic modelling. Accordingly, to develop general rheologic models, a family of curves has been drawn for each data set. These are shown as solid curves in Figs. 5–7. The low and high porosity curves approximate the range of data, whereas the intermediate curve is considered to best represent the data set as a whole. These curves are extrapolated to

cover the wide stresss/depth range of interest by maintaining approximate parallelism with data curves. The curves fitted with the hyperbolic stress–strain relationship are those for field shale, laboratory clay, and laboratory sand. The field sandstone data are not modelled because, as suggested above, porosity reduction below shallow depths is probably controlled by cementation or pressure solution. Slope of the porosity–depth curve is particularly variable at great depth (or equivalent depth) for field shale and laboratory clay. There is no discernible control of slope by either grain size or mineralogy and in the case of laboratory clays we gave greatest weight to natural sediments collected in the field in constructing the intermediate curve which is used in most calculations below.

For purposes of model calibration, the data to be fitted are stresses and strains, observed or inferred. The strength and deformation parameters to be determined are c, ϕ, R_f, k, ν and n. Assumptions and constraints are discussed below for each class of parameters.

Stress and strain

Effective vertical stresss σ_v (effective stress in the direction of compaction) is known for laboratory tests. For field data, depth is related to vertical stress by Eaton's (1969) vertical stress gradient curve for the U.S. Gulf Coast and an assumed pore pressure gradient of 0.0105 Mpa m^{-1}. This ignores the effect of overpressuring which, as discussed above, may be locally significant. Effective horizontal stress, σ_h for the field shale porosity–depth curves, was calculated according to Pilkington's (1978) relationships based on hydrofracturing data.

For curves derived from laboratory one-dimensional consolidation tests, σ_h is estimated as (Jaky 1944):

$$\sigma_h = \sigma_v(1 - \sin\phi), \tag{6}$$

where ϕ is friction angle for the sediment. This relationship, routinely employed in soil mechanics, characterizes horizontal stress in one-dimensional consolidation for both sand and clay (Mayne & Kulhawy 1982). It is used in this investigation because σ_h was not measured for most of the available test data. As indicated below, a single value of ϕ was used for all sands and a different value for all clays. The constant ratio of σ_v to σ_h implied by equation 6 is approximately confirmed experimentally to σ_v of 35 MPa by Karig & Hou (1992).

Strain at a given depth is calculated from the nine porosity–depth curves (solid curves of Figs. 5–7) under the assumption that all change in porosity results from vertical strain. The finite strain equation applied to the porosity–depth curves is:

$$\epsilon_z = \ln\left(\frac{(1 - p_f)}{(1 - p_i)}\right), \tag{7}$$

where p_i and p_f are initial and final porosities, respectively.

Strength and deformation parameters

Although it would be possible to find best fits for all parameters in the hyperbolic stress–strain model, both the limitations of the data and the intended use of the models argue against this. Stress–strain behavior in one-dimensional consolidation lies between elastic behavior and fully plastic yielding. For that reason, it is not well suited to determination of the Mohr–Coulomb strength parameters c and ϕ. With independent estimates of these parameters, a model is derived that should behave realistically under loading conditions closer to the Mohr–Coulomb failure envelope than those found in one-dimensional consolidation.

Sand is a cohesionless material ($c = 0$) well characterized by ϕ. Friction angle varies with density of the sand (i.e. closeness of packing) and with angularity of grains (Bishop & Eldin 1953, Leonards 1962, Sowers 1979, pp. 197–202). It exhibits minor variation with depth (Ladd et al. 1977), but for simplicity, a constant value is used in all analyses. Mayne & Kulhawy (1982) compiled data for 74 natural sands and artificial sands composed of natural sand grains. The mean of ϕ of $35.8°$ (s.d. $5.4°$) used in all calculations is approximately equidistant from the maximum and minimum values reported by Bishop & Eldin (1953) for different degrees of packing density. For clays and shales, shear strength τ is characterized by:

$$\tau = c + \sigma \tan \phi, \tag{8}$$

where σ is normal stress on the plane of failure and c is cohesion. A fundamental observation in soil mechanics is that for normally consolidated sediments, $c = 0$ and equation (8) reduces to:

$$\tau = \sigma \tan \phi. \tag{9}$$

This result, first recognized by Hvorslev (Hvorslev 1936, 1937, Tschebotarioff 1951, pp. 154–156), has been confirmed experimentally and is still considered valid (e.g. Leonards 1962, Peck 1985, Wroth & Houlsby 1985). Thus, strength of normally consolidated sediments is characterized by ϕ. This assumption is appropriate for modelling porosity reduction with burial and other deformation for which normal consolidation is maintained. For situations in which unloading has occurred, the sediment will be overconsolidated and equation (8), with non-zero c, will govern failure of clays and shales.

Mayne & Kulhawy's (1982) compiled ϕ angles for normally consolidated clays include both pure clays and more heterogeneous natural sediments described as clays. The ϕ angle tends to be lowest for pure expandable clays, as expected, but ϕ correlates only weakly with reported grain size parameters (Mayne & Kulhawy 1982). A mean ϕ of $26.5°$ (s.d. $5.6°$), calculated from 43 values (after deleting organic and glacial sediments) was used to characterize strength of clay and shale.

Procedure for material parameter determination

To find the best model for each of the nine porosity–depth curves, deformation parameters k, n, R_f and v, were allowed to vary within wide limits dictated by physical constraints. Each of the porosity–depth curves represents a hypothetical history of horizontal and vertical stresses and corresponding vertical strains. Knowledge of c, ϕ and vertical and horizontal effective stresses σ_v and σ_h and assumed trial values for k, n, R_f and v, allows calculation of E_t, for stress states corresponding to any depth by equation (5). Vertical and horizontal strain increments Δe_z and Δe_x are then calculated for each depth interval by incremental elastic stress–strain relationships:

$$\Delta \varepsilon_z = \left(\frac{1}{E_t}\right)[\Delta \sigma_z - 2v\Delta \sigma_x] \tag{10}$$

$$\Delta \varepsilon_x = \left(\frac{1}{E_t}\right)[(1 - v)\Delta \sigma_x - v\Delta \sigma_z], \tag{11}$$

where horizontal stress increments are assumed equal in the x and y directions. The stress–strain history for a particular trial hyperbolic stress–strain model is simulated by summing strain increments (equations 10 & 11) for 100 stress/depth increments. The error between strains calculated by the model and strains calculated directly from the porosity–depth curve is evaluated at approximately 15 points, equally spaced along the semilogarithmic porosity–depth curve. The logarithmic scale of the plots gives greater weight to the low stress (shallow depth) region of the curves where larger strains occur. For tectonically quiescent basins, horizontal strains ε_x and ε_y should be much less than ε_z and their correct value is assumed to be zero. Thus, to evaluate error at a point on the porosity–depth curve, twice the absolute value of horizontal strain calculated by equation (11) is added to the absolute value of the error for ε_z, and the sum is squared. Quality of fit for a model is judged by the sum of these squared errors.

The best model for each of the nine porosity–depth curves is found by a direct grid search using all combinations of the selected parameter values for k, n, R_f and v. The grid search is repeated several times in the neighborhood of the best-fitting model, with progressively smaller increments of the fitting parameters.

IMPLICATIONS OF THE HYPERBOLIC STRESS–STRAIN MODELS

Best-fitting material parameters for the nine porosity–depth curves are shown in Table 2. Stress–strain curves calculated directly from porosity–depth curves are compared to those calculated with the best-fitting model for the field shale intermediate porosity curve in Fig. 10. Behavior for other models is similar. The curves show both the profound non-linearity of the stress–strain curves and the good fit for geologically significant stresses. The graph on the right shows stress plotted on a logarithmic scale; it is apparent from this figure that the quality of fit is lowest at very low stresses. Kondner (1963) and Kondner & Zelasko (1963) also noted this

Table 2. Best-fitting parameters for hyperbolic stress–strain models

	k	n	R_f	ν
Shale (field)				
Low porosity	61.1	0.860	0.900	0.347
Intermediate porosity	27.6	0.819	0.824	0.363
High porosity	14.4	0.772	0.640	0.355
Clay (laboratory)				
Low porosity	38.3	0.846	0.692	0.363
Intermediate porosity	18.0	0.908	0.532	0.355
High porosity	22.5	0.969	0.984	0.355
Sand (laboratory)				
Low porosity	387.5	0.554	0.920	0.298
Intermediate porosity	214.5	0.656	0.760	0.298
High porosity	123.2	0.792	0.820	0.298

All parameters are dimensionless.

shortcoming of the hyperbolic stress–strain model. For clays and shales k is low, and n is relatively high resulting in very low E_t at shallow depths and a large increase in E_t with depth. For sands k is greater, and n smaller causing relatively large E_t at shallow depths and a smaller rate of increase with depth.

Variation of E_t with depth is shown in Fig. 11. The curves are calculated by equation (5), using the fitting parameters listed in Table 2 and effective vertical and horizontal stresses discussed above (Eaton 1969, Pilkington 1978). The variation in E_t is great between the low, intermediate and high porosity curves for a given data set. However, the intermediate curves for field shale and laboratory clay, which are relatively well constrained by the data, are almost identical.

The model's predictions of tangent modulus for uncemented sandstone and shale have interesting implications for folding analysis. Figure 11 indicates that tangent modulus is generally greater for sandstone than for clays and shales. The ratio of E_t for laboratory sand data ($E_{sandstone}$) to that for field shale and laboratory clay (E_{shale}) is plotted in Fig. 12. The figure shows that for field shale $E_{sandstone}/E_{shale}$ is 33 at 50 m depth, it decreases to 10 at 500 m and finally to 3 at 5 km. This convergence of effective tangent moduli at depth suggests that the thickness of individual sandstone beds may control folding wavelength at shallow depths where rheologic contrast is high. Where rheologic contrast is lower, a thick sandstone–shale sequence is less likely to fold, but it may fold as a single unit if it is bounded by incompetent units such as evaporites or overpressured shales.

Limitations of the models

Some limitations are intrinsic to the hyperbolic stress–strain formulation, others arise from limitations of the calibration data. The hyberbolic stress–strain models presented here are most appropriate for stress states in which sediments remain normally consolidated. If either σ_3 or σ_1 decreases, as during uplift and erosion, the sediments become overconsolidated; c then becomes non-zero for shales and other parameters also may

change. The models seem appropriate for simulating the continuum deformation observed in the Mexican Ridges Foldbelt, where throughout the history of sedimentation and deformation both σ_1 and σ_3 have increased monotonically, except in the up-dip region of growth faulting. This preserves the normally consolidated state in the folded region.

As formulated here the hyperbolic stress–strain law ignores anisotropy. This could be incorporated into the model by adding material parameters (Duncan & Chang 1970), however, their evaluation would require extensive data for multiaxial loading. As shown below, the anisotropy resulting from interlayering of sandstone and shale can be represented. Some potential error in the models is related to uncertainties in pore pressure. Pore pressure values in the field shale data are unknown. If high, they could cause shale stiffness to be overestimated or they could mask a small time-dependent component of strain.

MODELLING OF MEXICAN RIDGES WAVELENGTHS

Fold wavelength is a function of thicknesses and rheologies of the folding and underlying units. The turbidite units (Table 1) are assumed to be interbedded sandstones and shales and the pelagic and hemipelagic units are assumed to be shale. For each seismically recognizable unit in each of the four seismic lines (Fig. 1) we estimated the percentage of the unit with sand-prone characteristics such as clinoforms and discontinuous reflectors (Scarbrough 1992). This represents a crude quantitative assessment of the relative lithologic character of the units, but even in units judged to have a large percentage of sand-prone seismic facies the actual sandstone fraction is quite uncertain and may be small. The Mexican Ridges are on the continental slope, which might suggest a total sandstone fraction of less than 10% (Curtis & Picou 1978). However, some units may represent the distal part of submarine fans; parts of the analogous Mississippi fan are more than 50% sand at water depths exceeding those for Mexican Ridges deposition (Bouma et al. 1986).

Alternative lithologic models, intended to span the range of uncertainity, result from assigning various sandstone fractions to our numerical estimates of the percentage of sand-prone facies. Figure 13 shows a representative lithologic model which will be referred to below as the 'high sandstone' model (9.8% sandstone in the folded section). The 'low sandstone' model referred to below (2.5% sandstone) has (in each partly sandstone unit) 1/4 the sandstone fraction shown in Fig. 13.

A common element in all recent interpretations of the origin of the Mexican Ridges foldbelt is that the lower part of the sedimentary section is largely overpressured shale. Based on the change in seismic character and velocity Scarbrough (1992) places the top of the overpressured section at a depth of 2120 m in the study section for GLG-18 and at similar depth in the other
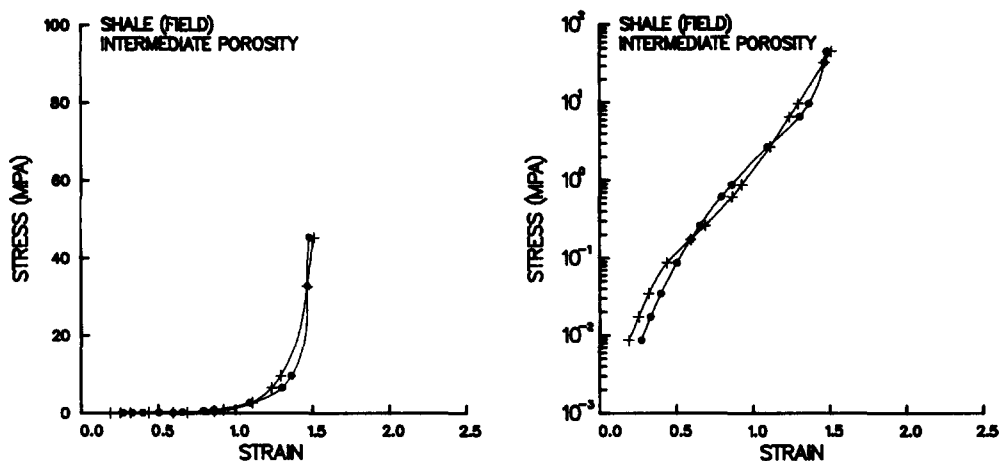
Fig. 10. Representative comparison of stress–strain curves calculated from porosity–depth curves (+) and from best-fitting hyperbolic stress–strain models (solid circles) with stress on a linear or logarithmic scale.
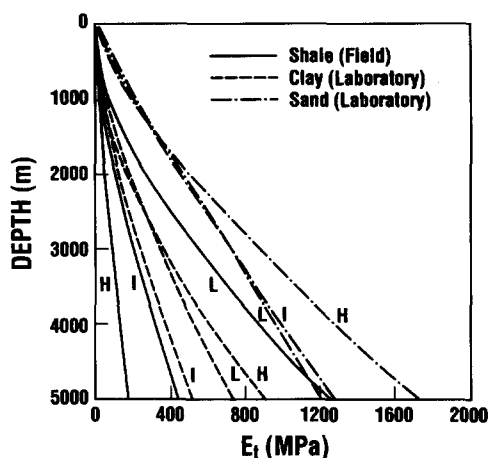

Fig. 11. Tangent modulus E_t vs depth for best-fitting models with *in situ* stress conditions. H, I and L refer to high, intermediate and low porosity models (Table 2) as defined by the solid curves in Figs. 5–7.
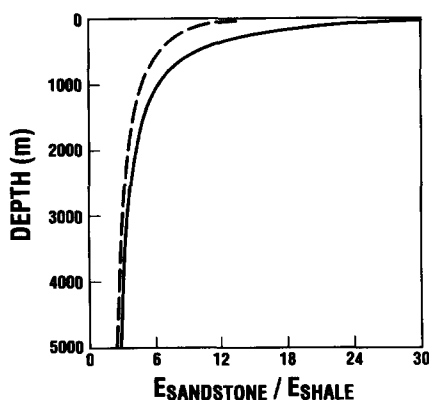

Fig. 12. Ratio of sandstone tangent modulus to moduli for field shale and clay (solid curve) and laboratory clay (dashed curve), computed from best-fitting hyperbolic stress–strain models for intermediate porosity.

seismic lines. Two alternative pore pressure distributions were used to represent overpressuring. Detailed measurements in other basins commonly reveal a normally pressured section overlying a seal across which there is a pressure jump (Hunt 1990, Powley 1990). Both above and below the seal the pressure gradient is hydrostatic. This model will be referred to as the sealed, normal gradient model. In this situation the highest

value of λ, pore pressure/lithostatic pressure, is directly below the seal. The result is a thin zone of reduced tangent modulus and reduced strength.

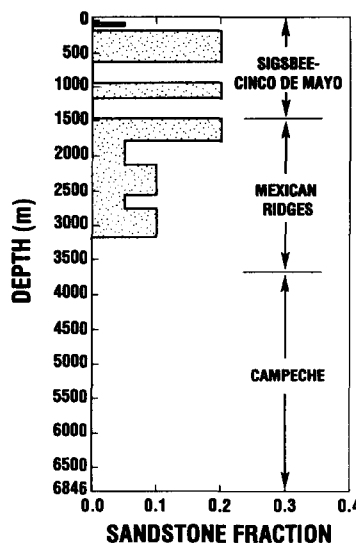In the second pore pressure model, pressure is normal

Fig. 13. Distribution of sandstone fraction for the high sandstone model, GLG-18.

near the surface, but is assumed to jump at some depth to a high and constant value of λ which then obtains below that depth. This implies a lithostatic pore pressure gradient if $\lambda = 1$ and a gradient between hydrostatic and lithostatic for more moderate values. This model will be referred to as the sealed, high gradient model. It seems a reasonable if overly simple model for a thick basal shale with low permeability. For this model the depth interval of relatively low stiffness and strength is thicker than for the sealed, normal gradient model.

The purpose of the finite element analysis was to find initial dominant wavelengths of folding. The dominant wavelength is determined for a particular lithologic and pore pressure model by subjecting finite element meshes with initial perturbations of different wavelength to horizontal shortening. The ratio of perturbation height to wavelength for the initial perturbation is the same for all models, and the dominant wavelength is that for which fold amplification, i.e. the ratio of folding deflection to initial perturbation, is maximum.

For each finite element mesh the horizontal dimension is half the assumed wavelength. The model extends down to the top of the Challenger Unit at which vertical displacement is assumed to be zero. The finite element mesh is shown in Fig. 14. The eight-node isoparametric elements used (Zienkiewicz 1971, p. 129–155) allow a quadratic (parabolic) displacement variation along the element. This allows accurate modelling of fold displacements with few elements. Element stiffness is numerically integrated with nine Gauss points rather than the minimal four to more accurately represent spacial variation of tangent modulus. The finite element code was written by the first author and executed in double precision on an IBM 3090. Isostatic stiffness (Tharp 1985) is imposed at the top of the mesh to account for the gravitational force resulting from vertical deflection of the sea bottom. Although for the 'at rest' condition in sedimentary basins vertical stress probably exceeds horizontal stress (Karig & Hou 1992), Mexican Ridges folding implies that horizontal stress has come to exceed vertical stress. For simplicity, we calculate tangent modulus for horizontal stress equal to vertical stress in all units.

Each lithologic unit is assumed to be all shale or interbedded sandstone and shale. Interbedded units are orthotropic, with different elastic properties parallel and perpendicular to bedding. In interbedded units, stiff sandstone beds carry greater horizontal stress than shale beds in response to horizontal strain, but both lithologies must have the same vertical stress. As a result Young's modulus in the horizontal direction will exceed that in the vertical direction. Even vertical strain in the shale is restricted by the sandstone beds because vertical strain engenders horizontal strain by Poisson's effect and the sandstone beds constrain that deformation. Thus the increase in stiffnesses, particularly horizontal stiffness, caused by a modest sandstone fraction can be substantial where the rheologic contrast between sandstone and shale is high. There are five independent elastic constants for an orthotropic material. The rather involved algebraic expressions (not shown) are found in terms of the fractions of sandstone and shale and the isotropic elastic constants of the two lithologies by obvious simplifications of the general expressions derived by Gerrard (1982).

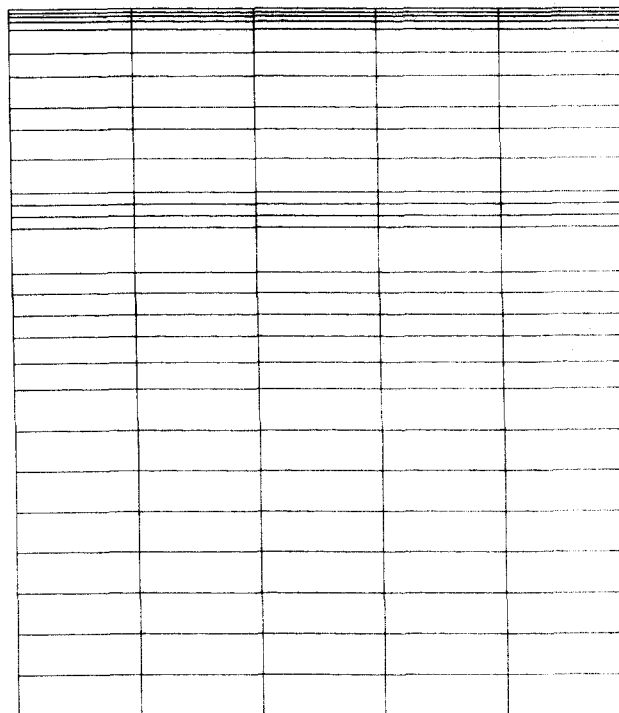Because only the initial dominant wavelength is inves-

Fig. 14. Finite element mesh with initial vertical sinusoidal perturbation of 0.01 times wavelength. The lower surface is fixed in the vertical direction, the right side of the mesh is fixed in the x direction and the left side has constant displacement in the x direction.
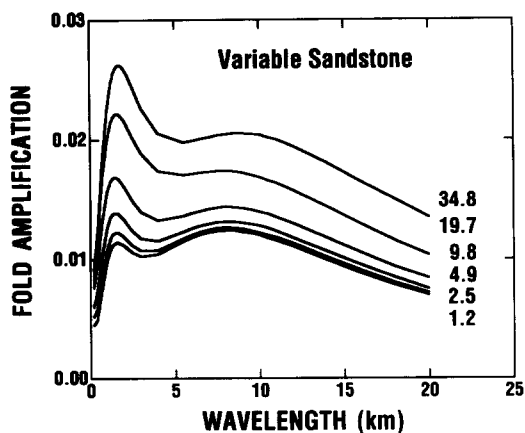
Fig. 15. Fold amplitude vs wavelength for variable sandstone fraction, shown as total sandstone percentage in the folded section. For all models the sealed, normal gradient pore pressure model with $\lambda = 0.9$ at the top of the overpressured section was used.

tigated a simple linear elastic analysis suffices. The elastic amplifications shown below are very small, but non-linear finite element analyses (work in progress) show that buckling forces and the non-linearity of the hyperbolic stress–strain law produce sufficient amplification to explain the observed folding. In non-linear analyses amplification increases at an accelerating rate with fold amplitude. With $\lambda = 0.95$ in the sealed, high gradient, high sandstone model horizontal shortening of 15% produces the 150 m fold relief of the highest amplitude folds in the study area from an initial perturbation of only 10 m over a wavelength of 10 km. Strain softening in the hinges of the folds maintains the dominant wavelength established initially, with a modest reduction occasioned by horizontal shortening.

INITIAL DOMINANT WAVELENGTHS

Variation of fold amplification with wavelength is shown in Figs. 15 and 16 and Table 3. The vertical displacements result from an arbitrary lateral strain of 0.01, imposed on a model with initial vertical sinusoidal perturbation of the mesh of 0.005 times assumed wavelength. For a wide variety of models there are two peaks in the fold amplification vs wavelength curve. These two peaks are observed when fold deflections are taken at the surface, but dominant wavelength and the relative intensity of the two fold wavelengths are more accurately represented by fold deflections measured closer to the neutral surface of each folding section. This is true because with Young's modulus increasing downward, the neutral surface of the folding section (i.e. the depth at which bending strain is zero) is shifted below the middle of the folding section. This attenuates displacements of both anticlinal and synclinal sense at the surface for the following reason. Bending strain increases linearly away from the neutral surface and at the same rate above and below. The part of the folding section above the neutral surface is thicker and, in a syncline, it is in compression, whereas the thinner part of the folding section below the neutral surface is in tension
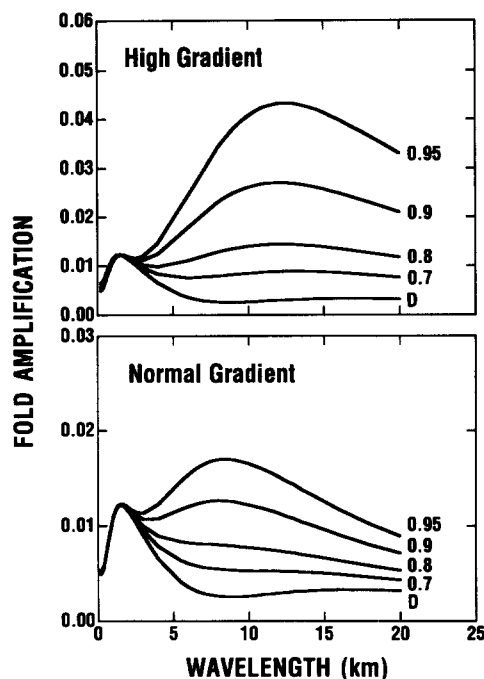

Fig. 16. Fold amplitude vs wavelength for the low sandstone model with variable λ (shown to right of each curve) for the sealed high gradient and sealed normal gradient pore pressure models. For curve 'D' the drained condition is assumed for the basal shale.

Table 3. Dominant wavelengths

λ	Shallow folds Wavelength (km)	Shallow folds A	Large folds Wavelength (km)	Large folds A
High pressure gradient, low sandstone				
0.95	1.50	1.23	11.5	5.64
0.9	1.55	1.23	10.5	3.83
0.8	1.55	1.22	10.0	2.41
0.7	1.60	1.22	10.0	1.79
High pressure gradient, high standstone				
0.95	1.45	1.69	12.0	5.96
0.9	1.45	1.69	10.5	4.09
0.8	1.45	1.69	10.5	2.61
0.7	1.45	1.69	10.5	1.96
Normal pressure gradient, low sandstone				
0.95	1.60	1.23	7.5	2.80
0.9	1.60	1.22	7.5	2.29
0.8	1.60	1.22	7.0	1.75
0.7	1.60	1.22	7.5	1.45
Normal pressure gradient, high sandstone				
0.95	1.45	1.69	8.0	2.95
0.9	1.45	1.69	8.0	2.44
0.8	1.45	1.69	8.0	1.89
0.7	1.45	1.69	8.0	1.60
Drained, low sandstone				
—	1.55	1.22	11.0	1.16
Drained, high sandstone				
—	1.45	1.69	9.5	1.29

A is amplification multiplied by 10^2.

(considering only bending strains). As a result, in a syncline both the average compressive strain and thickness of section in compression exceed the average magnitude of tensile strain and thickness of section in tension (below the neutral surface). Because compressive strain in the horizontal direction causes dilation in the vertical direction by Poisson's effect, this excess of compressive over tensile strain in a syncline causes a net vertical dilation. The same mechanism causes vertical contraction in anticlines, with the net result that fold amplitudes decrease upward away from the neutral surface. In extreme conditions, as when a thick shale at the surface is underlain by a folding sandstone the folds may die out or even reverse displacement at the surface.

The short wavelength second-order folds, seen in Fig. 2 and predicted by the models, are governed by and die out below the uppermost sand-prone unit which is of latest Miocene to Late Pliocene age (Bertagne 1984) and occurs in the depth interval 200–652 m in GLG-18 and at similar levels in the other profiles. The steep vertical gradient for E_t near the surface and the 200 m of shale-rich section above this sand-prone unit shifts the neutral surface deep below the surface and greatly attenuates folding displacement at the sea floor. To partly compensate for this effect all folding displacements in Figs. 15 and 16 are measured at a depth of 426 m, in the middle of the sand-rich unit that controls the second-order folds. It is puzzling that, where observed on the seismic sections, these folds do not exhibit this predicted upward attenuation. The attenuation may be an artifact of the linear analysis, but it is also possible that the surface shale may be at least partly younger than the second-order folds. Deposited from suspension, these shales could drape over the subdued topography of the folds with little thickening or thinning.

The downward shift of the neutral surface is less important for the large, first-order folds, but to allow comparison without the attenuation effect, dominant wavelengths and amplifications for large folds in Table 3 are based on fold displacements measured in the middle of the folding section (depth 1378 m). This results in larger amplification and smaller dominant wavelength than seen in Figs. 15 and 16. For the small folds, parameters in Table 3 result from displacements measured at 426 m, as in Figs. 15 and 16.

Effect of sandstone fraction

The most striking result of the analyses is that fold wavelength is only weakly a function of sandstone fraction in the folded section. Figure 15 shows amplification vs wavelength for GLG-18 models with sandstone fraction in the folded section ranging from 1.2–34.8% and λ = 0.9 for the sealed, normal gradient pore pressure model. Specific results for the other three seismic sections are not shown because in models for all combinations of sandstone fraction and pore pressure, dominant wavelengths depart from those for GLG-18 by only 20%. All calculations shown use the intermediate-porosity hyperbolic stress–strain models for laboratory
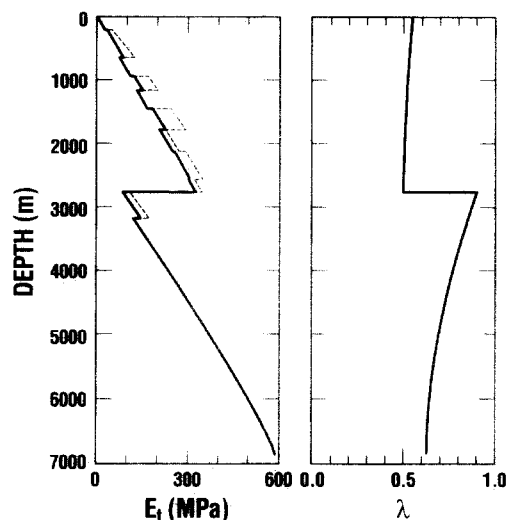

Fig. 17. Left tangent Young's modulus for low sandstone model (solid curve) and high sandstone model (dashed where it differs from low sandstone model). Right corresponding λ for sealed, normal gradient model with λ = 0.9 at top of overpressured section.

sand and clay. Dominant wavelengths for runs with high and low porosity models generally differ from intermediate porosity runs by less than 10%.

Dominant wavelength is insensitive to sandstone fraction for a number of reasons. Figure 17 shows distributions of E_t and λ for high and low sandstone models with the sealed, normal gradient pore pressure model and λ = 0.9 at the top of the overpressured zone. At moderate and greater depth the difference in elastic moduli between sandstone and shale is small and given the significant shale fraction even of sand-prone units, the contrast between relatively sand-rich and shale-rich units is small.

Simpler models confirm that only small changes in wavelength are expected for the calculated moduli. Dominant wavelength L for a single elastic layer embedded in an elastic medium is (Gough *et al.* 1940, Johnson 1977, p. 10):

$$L = 2\pi(t^3 B/6B_0)^{1/3}$$ (12)

which can be stated as:

$$L = 2\pi(2F/B_0)^{1/3},$$ (13)

where flexural rigidity $F = EI/(1-v^2)$, $B = E/(1-v^2)$ and $B_0 = E_0/(1-v_0^2)$, E and E_0 and v and v_0 are Young's moduli and Poisson's ratios of the elastic layer and infinite medium respectively, and $I = t^3/12$ is moment of inertia for the elastic layer of thickness t and unit width. Flexural rigidity for the folded section of GLG-18 is higher by a factor of 1.86 for 34.8% sandstone than for 1.2% sandstone. The cube root relationship of the single layer model (equation 13) predicts a dominant wavelength only 23% greater for the 34.8% sandstone model. Because dominant wavelength is linearly proportional to t but is proportional only to the cube root of (B/B_0), wavelength is largely governed by thickness of the folded section for the modest contrasts in modulus predicted by the hyperbolic stress–strain model for folding units extending to depths of several kilometers.

Because the Mexican Ridges folded section is a multilayer and because the modulus contrast with the underlying overpressured unit is small, the vertical compliance of the multilayer itself may be important in accommodating folding. Johnson (1977, pp. 25–74) found dominant wavelength L_m for a multilayer confined above and below by rigid, non-folding layers:

$$L_m = 2\pi(T/n\pi)^{1/2}\left(\frac{B_p t_1^3}{B_n t}\right)^{1/4}, \qquad (14)$$

where n is an integer equal to 1 for the relevant geometry, T is total thickness of the multilayer, t_1 is thickness of each stiff layer, t_1/t is the fraction of the multilayer that is stiff, B_p and B_n are elastic moduli parallel and normal to the layering, respectively. The moduli B_p and B_n are composites representing the effect of both soft and stiff layers. Increasing sandstone fraction from 1% to 50% increases the ratio of B_p/B_n from 1.004 to 1.087 at a depth of 1500 m, the approximate middle of the folding section. When taken to the 1/4 power, this difference produces only a 2% change in dominant wavelength. Thus for modulus values predicted by the hyperbolic stress–strain model, dominant wavelength should be only weakly influenced by the effect of sandstone fraction on vertical and horizontal compliances in the folding section.

The effect of sandstone fraction on dominant wavelength of the upper, small wavelength folds slightly exceeds that for the longer folds. The modulus contrast between sandstone and shale is higher near the surface, which increases the influence of sandstone fraction. It is notable that the folded sediments of the Mexican Ridges were deposited over a wide range of ocean depth and distance to the shelf. Given the extreme range of depositional environments it is probable that sandstone fraction varies along strike and downslope, and the predicted insensitivity of wavelength to sandstone fraction may account for the modest variation in wavelength across the foldbelt.

The greatest influence of sandstone fraction is on fold amplification rather than on dominant wavelength. For a constant λ the initial amplification is 45% higher for the highest sandstone model than for the lowest sandstone model for long wavelength folds. Range of initial amplification is far greater for the shallow folds, varying by a factor of 2.8. It is significant that small wavelength surface folds are most common in those parts of the four seismic sections where the clinoforms, indicative of high sand fraction, are well developed in the sand-prone unit found at 200–652 m depth in GLG-18.

The finite element models (Fig. 15) suggest also that the difference in amplification between short and long wavelength folds is strongly a function of sandstone fraction. The modulus contrast between sand-rich and sand-poor units is much greater near the surface, where the sand and shale moduli are very different. High sandstone fraction therefore enhances fold amplification more in the near-surface, short wavelength folds than in the long wavelength folds. The much greater

limb dips for long than short wavelength folds in the Mexican Ridges seem most consistent with a small sandstone fraction (Fig. 15). Although restriction of short wavelength folding to surface layers is favored by the downward reduction in modulus contrast between layers, surface folding in a multilayer is promoted also by the lack of constraint at the free surface. Ramberg (1970) demonstrated short wavelength surface folds superimposed on long wavelength folds in a multilayer overlying a less viscous substratum. The multilayer contained alternating soft and stiff units but neither changed with depth.

Effect of pore pressure

Increased pore pressure in the basal shale reduces its effective elastic modulus, increasing dominant wavelength as predicted by the single layer model (equation 12). In the sealed, high gradient models, dominant wavelength for the longer folds increases by 10–20% in going from $\lambda = 0.7$ to $\lambda = 0.95$ (Fig. 16 and Table 3). The increase is greatest for the high sandstone model (Table 3). The modest nature of the variation with pore pressure for both sandstone models is predicted by the single layer model (equation 12). An increase in pore pressure from $\lambda = 0.7$ to $\lambda = 0.95$ decreases effective Young's modulus by a factor of 2 at all depths in the basal shale. By equation (12) this would increase dominant wavelength by only 25%.

The pattern of dominant wavelength variation is similar for the sealed, normal gradient pore pressure models, but for these models the low modulus zone at the top of the basal shale is thinner (compare Fig. 18 with Fig. 17). This results in shorter dominant wavelength (Fig. 16 and Table 3). Because the small-scale folds are a near-surface phenomenon, their dominant wavelength is unaffected by pore pressures in the basal units.

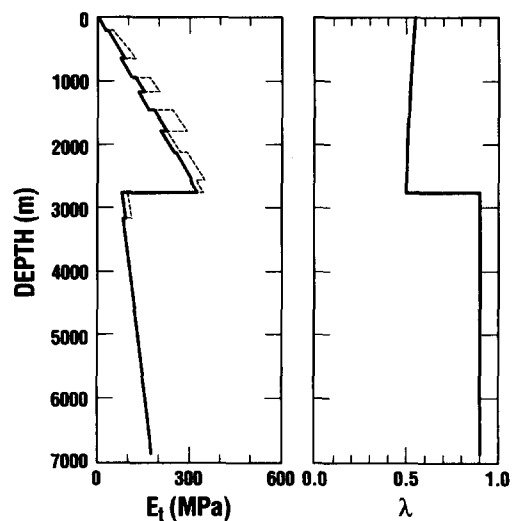Although dominant wavelength is little affected by

Fig. 18. Left tangent Young's modulus for low sandstone model (solid curve) and high sandstone model (dashed where it differs from low sandstone model). Right corresponding λ for sealed, high gradient model with $\lambda = 0.9$ in overpressured section.

pore pressure magnitudes in the basal shale and is only modestly affected by pore pressure distribution, amplification of long wavelength folds is greater for high pore pressures in the basal section (Fig. 16) whereas amplification of short wavelength folds is unaffected. The greater prominence of the long wavelength folds is most consistent with high pore pressure, although as discussed above, small sandstone fraction could also be responsible for this difference.

Comparison with Mexican Ridges folding

The Mexican Ridges are low amplitude folds and have probably experienced only modest reduction of wavelength by shortening. Pew (1982) estimated shortening to be 1–2%, but did not include layer-parallel shortening which, based on non-linear analyses, could give total shortening of the order of 15%. Observed wavelengths (Fig. 3) are generally consistent with initial dominant wavelengths predicted by the finite element study. The broad peaks in the histogram (Fig. 3) also are consistent with the broadness of peaks in fold amplification found in the numerical models (Fig. 16). Given this limited wavelength selectivity, and variation in the models, adjusting wavelengths for the probable modest shortening would have little apparent effect on the correlation between calculated and observed wavelengths.

Pew (1982) noted a general downslope increase in fold wavelength. The histogram (Fig. 3) shows a strong wavelength peak at 7 km that represents the upslope folds, and a secondary wavelength peak at 10 km, which is dominated by downslope folds. Although uncertainties argue for coincidence rather than correlation, these two peaks correspond approximately to the two pore pressure models presented. This observation fits into a plausible if speculative interpretation of wavelength in the Mexican Ridges. As shown, a downslope decrease in sandstone fraction would have little direct effect on wavelength of long folds. However, such a trend might be associated with higher pore pressures downslope and perhaps a tendency for development of the sealed, high gradient pore pressure condition that would favor the observed longer wavelengths. A decreasing sandstone fraction downslope also would be consistent with the observed small reduction in fold amplitude. Downslope reduction in horizontal stress in the folded units, caused by shear resistance on their base, could also be important. This would decrease horizontal shortening downslope and might account for part of the increase in wavelength.

CONCLUSIONS

The hyperbolic stress–strain models provide good fits to porosity–depth curves for both sandstone and shale. They are accurate for geologically interesting depth ranges over which stress–strain relationships are extremely non-linear. The models show a large increase in E_t with depth for both sandstone and shale, but because

the increase is greater for shale the ratio $E_{sandstone}/E_{shale}$ decreases sharply with depth. This change may promote short folds with wavelength governed by individual sandstone beds near the surface, whereas at greater depth, interbedded sandstone and shale sections may fold as single units. This effect may contribute to the presence of short wavelength, shallow folds superimposed on long wavelength, deep folds in the Mexican Ridges.

The simulations of Mexican Ridges folding suggest some additional general observations. An important conclusion is that for the elastic moduli expected for normally consolidated sandstone–shale sequences, fold wavelengths can be fairly accurately predicted if the thickness of folding layers is known. Equations (12) and (13) for simple systems illustrate the minor influence of modulus variations within their probable range and the concomitant importance of layer thicknesses. The tendency to fold is probably more strongly influenced by possible modulus variations than is fold wavelength. Although the evolution of folding is beyond the scope of this paper, it is clear that fold amplification is strongly a function of modulus contrasts, whether caused by lithologic or pore pressure contrast.

The linear elastic analysis answers only a few questions about folding in the Mexican Ridges. A more complete understanding will require analysis of the entire continental slope and adjacent regions with gravitational driving forces, geometric nonlinearity, incremental application of the hyperbolic stress–strain law, and coupling with pore pressure.

REFERENCES

Allen, D. R. & Chilingarian, G. V. 1975. Mechanics of sand compaction. In: *Compaction of Coarse-Grained Sediments, I* (edited by Chilingarian, G. V. & Wolf, K. H.). Elsevier, New York, 43–78.

Allen, D. R. & Mayuga, M. N. 1969. The mechanics of compaction and rebound, Wilmington Oil Field, Long Beach, California. In: *Land Subsidence*. IASH-UNESCO, Tokyo, **89**(2), 410–413.

Bertagne, A. J. 1984. Seismic stratigraphy of Veracruz Tongue, deep southwestern Gulf of Mexico. *Bull. Am. Ass. Petrol. Geol.* **68**, 1894–1907.

Bishop, A. W. & Eldin, A. K. G. 1953. The effect of stress history on the relation between ϕ and porosity in sand. *Proc. Third Int. Conf. Soil Mech. Found. Engr.* Zurich **1**, 100–105.

Boatman, W. A., Jr. 1967. Measuring and using shale density to aid in drilling wells in high-pressure areas. *J. Petrol. Tech.* **21**, 1423–1429.

Bouma, A. H., Coleman, J. M. & Meyer, A. W. 1986. Introduction, objectives, and principal results of Deep Sea Drilling Project Leg 96. *Init. Repts. DSDP* **96**, 15–36.

Bouma, A. H., Sweet, W. E. Jr., Dunlap, W. A. & Bryant, W. R. 1972. Comparison of geological and engineering parameters of marine sediments. Fourth Annual Offshore Technology Conference, Houston, TX, May 1, Paper OTC-1514.

Brown, P. R. 1969. Compaction of fine-grained terrigenous and carbonate sediments—a review. *Bull. Can. Petrol. Geol.* **17**, 486–495.

Bryant, W. R., Antoine, J. W., Ewing, M. & Jones, B. 1968. Structure

of the Mexican continental shelf and slope, Gulf of Mexico. *Bull. Am. Ass. Petrol. Geol.* **52**, 1204–1228.

Bryant, W. R., Cernock, P. & Morelock, J. 1967. Shear strength and consolidation characteristics of marine sediments from the western Gulf of Mexico. In: *Marine Geotechnique* (edited by Richards, A. F.). Univ. of Ill. Press, 22–40.

Bryant, W. R., Deflache, A. P. & Trabant, P. K. 1974. Consolidation of marine clays and carbonates. In: *Deep Sea Sediments* (edited by Inderbitzen, A.). Plenum Press, New York, 209–244.

Bryant, W. R., Hottman, W. & Trabant, P. 1975. Permeability of unconsolidated and consolidated marine sediments, Gulf of Mexico. *Marine Geotechnol.* **1**, 1–14.

Bryant, W. R., Lugo, J., Cordova, C. & Salvador, A. 1991. Physiography and bathymetry. In: *The Gulf of Mexico Basin* (edited by Salvador, A.). Geol. Soc. Am., The Geology of North America, v. J. 13–30.

Buffler, R. T. 1991. Seismic stratigraphy of the deep Gulf of Mexico basin and adjacent margin. In: *The Gulf of Mexico Basin* (edited by Salvador, A.). Geol. Soc. Am., The Geology of North America, v. J, 353–387.

Buffler, R. T., Shaub, F. J., Watkins, J. S. & Worzel, J. L. 1979. Anatomy of the Mexican Ridges, southwestern Gulf of Mexico. In: *Geological and Geophysical Investigations of Continental Margins* (edited by Watkins, J. S., Montadert, L. & Dickerson, P. W.). *Mem. Am. Ass. Petrol. Geol.* **29**, 319–327.

Chilingarian, G. V. & Knight, L. 1960. Relationship between pressure and moisture content of kaolinite, illite and montmorillonite clays. *Bull. Am. Ass. Petrol. Geol.* **44**, 101–106.

Curtis, D. M. & Picou, E. B., Jr. 1978. Gulf Coast Cenozoic; a model of the application of stratigraphic concepts to exploration on passive margins. *Trans. Gulf Coast Ass. geol. Soc.* **28**, 103–120.

Das, B. M. 1983. *Advanced Soil Mechanics.* McGraw-Hill, New York.

Davis, D., Suppe, J. & Dahlen, F. A. 1983. Mechanics of fold-and-thrust belts and accretionary wedges. *J. geophys. Res.* **88**, 1153–1172.

Dickey, P. A. 1972. Migration of interstitial water in sediments and the concentration of petroleum and useful minerals. *Proc. Twenty-fourth Int. Geol. Congr.*, 3–16, Montreal.

Dickinson, G. 1953. Geological aspects of abnormal reservoir pressures in Gulf Coast Louisiana. *Bull. Am. Ass. Petrol. Geol.* **37**, 410–432.

Duncan, J. M. 1981. Hyperbolic stress-strain relationships. In: *Limit Equilibrium, Plasticity and Generalized Stress-Strain in Geotechnical Engineering* (edited by Yong, R. K. & Ko, H.-Y.). Am. Soc. Civ. Engr., New York, 443–460.

Duncan, J. M. & Chang, C.-Y. 1970. Nonlinear analysis of stress and strain in soils. *J. Soil Mech. Found. Engr.*, Am. Soc. Civ. Engr. **96**, 1629–1653.

Eaton, B. A. 1969. Fracture gradient propagation and its application in oilfield operations. *J. Petrol. Tech.* **21**, 1353–1360.

Emery, K. O. & Rittenberg, S. C. 1952. Early diagenesis of California basin sediments in relation to origin of oil. *Bull. Am. Ass. Petrol. Geol.* **36**, 735–806.

Emery, K. O. & Uchupi, E. 1972. Western North Atlantic Ocean: Topography, rocks, structure, water, life and sediments. *Mem. Am. Ass. Petrol. Geol.* **17**.

Ewing T. E. 1991. Structural framework. In: *The Gulf of Mexico Basin* (edited by Salvador, A.). Geol. Soc. Am., The Geology of North America, v. J. 31–52.

Foster, J. B. & Whalen, H. E. 1966. Estimation of formation pressures from electrical surveys—Offshore Louisiana. *J. Petrol. Tech.* **18**, 165–171.

Fuchtbauer, H. 1967. Influence of different types of diagenesis on sandstone porosity. *Proc. Seventh World Petrol. Congr.* **2**, 353–369.

Galloway, W. E. 1974. Deposition and diagenetic alteration of sandstone in NE Pacific arc-related basins: implications for greywacke diagenesis. *Bull. geol. Soc. Am.* **85**, 379–390.

Garrison, L. E. & Martin, R. G., Jr. 1973. Geologic structures in the Gulf of Mexico basin. U.S. Geol. Surv. Prof. Paper 773.

Gerrard, C. M. 1982. Equivalent elastic moduli of a rock mass consisting of orthorhombic layers. *Int. J. Rock Mech. Min. Sci. & Geomech. Abstr.* **19**, 9–14.

Gilboy, G. 1928. The compressibility of sand-mica mixtures. *Proc. Am. Soc. Civ. Engr.* **54**, 555–568.

Gough, G. S., Elan, C. F. & DeBruyne, N. A. 1940. The stabilization of a thin sheet by a continuous supporting medium. *J. R. Aeronaut. Soc.* **44**, 12–43.

Gould, H. R. 1960. Character of the accumulated sediment. In: *Comprehensive Survey of Sedimentation in Lake Mead, 1948–1949.* U.S. Geol. Surv. Prof. Pap. 295.

Gratz, A. J. 1991. Solution transfer compaction of quartzites: progress toward a rate law. *Geology* **19**, 901–904.

Griffin, D. G. & Bazer, D. A. 1969. A comparison of methods for calculating pore pressures and fracture gradients from shale density measurements using the computer. *J. Petrol. Tech.* **21**, 1463–1473.

Hedberg, H. D. 1936. Gravitational compaction of clays and shales. *Am. J. Sci.* **31**, 241–287.

Heling, D. 1969. Relationships between initial porosity of Tertiary argillaceous sediments and paleosalinity in Rheintalgraben (SW Germany). *J. sedim. Petrol.* **39**, 246–254.

Houseknecht, D. W. 1988. Intergranular pressure solution in four quartzose sandstones. *J. sedim. Petrol.* **58**, 228–246.

Hsu, K. J. 1977. Studies of Ventura field, California: II: lithology, compaction, and permeability of sands. *Bull. Am. Ass. Petrol. Geol.* **61**, 169–191.

Hunt, J. M. 1990. Generation and migration of petroleum from abnormally pressured fluid compartments. *Bull. Am. Ass. Petrol. Geol.* **74**, 1–12.

Hvorslev, M. J. 1936. Conditions of failure for remolded cohesive soils. *Proc. First Int. Conf. Soil Mech. Found. Engr.* **3**, 51–53.

Hvorslev, M. J. 1937. Uber die festigkeitseigenschaften gestorter bindiger boden (On the strength characteristics of remolded cohesive soils). *Ingeniorvidenkabalige Skrifter*, ser. A, no. 35.

Jaky, J. 1944. The coefficient of earth pressure at rest. *Magyar menok es epitesz egylet kozloi* (J. Soc. Hung. Archit. Engr.), 355–358.

Johnson, A. M. 1977. *Styles of Folding.* Elsevier, Amsterdam.

Jones, B. R., Antoine, J. W. & Bryant, W. R. 1967. A hypothesis concerning the origin and development of salt structures in the Gulf of Mexico sedimentary basins. *Trans. Gulf Coast geol. Soc.* **17**, 211–216.

Jones, M. E. & Addis, M. A. 1986. The application of stress path and critical state analysis to sediment deformation. *J. Struct. Geol.* **8**, 575–580.

Karig, D. E. & Hou, G. 1992. High-stress consolidation experiments and their geologic implications. *J. geophys. Res.* **97**, 289–300.

Keller, G. H. & Bennett, R. H. 1973. Sediment mass physical properties—Panama Basin and Northeastern Equatorial Pacific. In: *Initial Reports of the Deep Sea Drilling Project*, 16 (edited by van Andel, T. H. *et al.*). U.S. Govt. Printing Office, Washington, D.C., 499–512.

Kharaka, Y. K. & Berry, F. A. F. 1976. Chemistry of waters expelled from sands and sandstones. In: *Compaction of Coarse-Grained Sediments, II* (edited by Chilingarian, G. V. & Wolf, K. H.). Elsevier, New York, 41–68.

Kidwell, A. L. & Hunt, J. M. 1958. Migration of oil in recent sediments of Pedernales, Venezuela. In: *Habitat of Oil* (edited by Weeks, L. G.). Am. Ass. Petrol. Geol. Tulsa, Oklahoma, 790–817.

Kondner, R. L. 1963. Hyperbolic stress–strain response: Cohesive soils. *J. Soil Mech. Found. Engr.*, Am. Soc. Civ. Engr. **89**, 115–143.

Kondner, R. L. & Zelasko, J. S. 1963. A hyperbolic stress–strain formulation for sands. *Proc. Second Panamerican Conf. Soil Mech. Found. Engr.* Associacao Brasileira de Mecanica de Solos, Brasil **1**, 290–324.

Kosloff, D., Scott, R. F. & Scranton, J. 1980. Finite element simulation of Wilmington oil field subsidence: Nonlinear modelling. *Tectonophysics* **70**, 159–183.

Ladd, C. C., Foott, R., Ishihara, K., Schlosser, F. & Poulos, H. G. 1977. Stress-deformation and strength characteristics. In: *Proc. Ninth Int. Conf. Soil Mech. Found. Engr.* Tokyo **2**, 421–494.

Land, L. S. 1984. Frio sandstone diagenesis, Texas Gulf Coast: a regional isotopic study. In: *Clastic Diagenesis* (edited by McDonald, D. A. & Surdam, R. C.). *Mem. Am. Ass. Petrol. Geol.* **37**, 47–62.

Leonards, G. A. 1962. Engineering properties of soils. In: *Foundation Engineering* (edited by Leonards, G. A.). McGraw-Hill, New York, 66–240.

Loucks, R. G. & Dodge, M. M. 1980. Analysis of Texas Gulf Coast Tertiary sandstones to delineate areas of high-quality geopressured geothermal reservoirs. In: *Proc. Fourth U.S. Gulf Coast Geopressured-Geothermal Energy Conference: Research and Development, I,* (edited by Dorfman, M. H. & Fisher, W. L.). Center for Energy Studies, Univ. of Texas at Austin, 373–413.

Loucks, R. G., Dodge, M. M. & Galloway, W. E. 1979. Importance of secondary leached porosity in lower Tertiary sandstone reservoirs along the Texas Gulf Coast. *Trans. Gulf Coast Ass. geol. Soc.* **29**, 164–171.

Loucks, R. G., Dodge, M. M. & Galloway, W. E. 1984. Regional controls on diagenesis and reservoir quality in lower Tertiary sand-

stones along the Texas Gulf Coast. In: *Clastic Diagenesis* (edited by McDonald, D. A. & Surdam, R. C.). *Mem. Am. Assoc. Petrol. Geol.* **37**, 15–45.

Loucks, R. G., Richmann, D. L. & Milliken, K. L. 1981. Factors controlling porosity and permeability in geopressured Frio sandstone reservoirs, General Crude Oil/Department of Energy Pleasant Bayou test wells, Brazoria County, Texas. In: *Proc. Fourth U.S. Gulf Coast Geopressured–Geothermal Energy Conference: Research and Development*, 1, (edited by Dorfman, M. H. & Fisher, W. L.). Center for Energy Studies, Univ. of Texas at Austin, 46–84.

Magara, K. 1968. Compaction and migration of fluids in Miocene mudstone, Nagaoka Plain, Japan. *Bull. Am. Ass. Petrol. Geol.* **52**, 2466–2501.

Magara, K. 1978. *Compaction and Fluid Migration: Practical Petroleum Geology.* Elsevier, Amsterdam.

Massengill, J. V., Bergantino, R. N., Fleming, H. S. & Feden, R. H. 1973. Geology and genesis of the Mexican Ridges: Western Gulf of Mexico. *J. geophys. Res.* **78**, 2498–2507.

Maxwell, J. C. 1964. Influence of depth, temperature and age on porosity of quartzose sandstone. *Bull. Am. Ass. Petrol. Geol.* **48**, 697–709.

Mayne, P. W. & Kulhawy, F. H. 1982. K_o-OCR relationships in soil. *J. Geotech. Engr. Am. Soc. Civ. Engr.* **108**, 851–873.

Meade, R. H. 1963. Factors influencing the pore volume of fine-grained sediments under low to moderate overburden loads. *Sedimentology* **2**, 235–242.

Nobes, D. C. 1986. Physical properties of clay-rich sediments: a database of Deep Sea Drilling Project results. Energy, Mines and Resour. Can., Earth Phys. Branch, Ottawa, Open File Rep. 86–3.

Nobes, D. C., Villinger, H., Davis, E. E. & Law, L. K. 1986. Estimation of marine sediment bulk physical properties at depth from seafloor geophysical measurements. *J. geophys. Res.* **91**, 14,033–14,043.

Oertel, G. 1983. The relationship of strain and preferred orientation of phyllosilicate grains in rocks—a review. *Tectonophysics* **100**, 413–447.

Peck, R. B. 1985. The last sixty years. In: *Proc. Eleventh Int. Conf. Soil Mech. Found. Engr.* Golden Jubilee Volume, Balkema, Rotterdam, 123–133.

Pew, E. 1982. Seismic structural analysis of deformation in the southern Mexican Ridges. M.S. Thesis, Univ. of Texas, Austin.

Philipp, W., Drang, H. J., Fuchtbauer, H., Haddenhorst, H. G. & Jankowsky, W. 1963. The history of migration in the Gifhorn Trough (NW Germany). Sixth World Pet. Congr., Sect. 1, pap, 19. 457–481.

Pilkington, P. E. 1978. Fracture gradient estimates in Tertiary basins. *J. Petrol. Engin. Int.* May, 138–148.

Powley, D. E. 1990. Pressures and hydrogeology in petroleum basins. *Earth Sci. Rev.* **29**, 215–226.

Ramberg, H. 1970. Folding of laterally compressed multilayers in the field of gravity, II numerical examples. *Phys. Earth & Planet. Interiors* **4**, 83–120.

Richards, A. F. & Keller, G. H. 1962. Water content variability in a silty clay core from off Nova Scotia. *J. Limnol. & Oceanogr.* **7**, 426–427.

Rieke, H. H. & Chilingarian, G. V. 1974. *Compaction of Argillaceous Sediments.* Elsevier, New York.

Roberts, J. E. 1969. Sand compression as a factor in oil field subsidence. In: *Land Subsidence.* IASH-UNESCO, Tokyo, **89**(2), 368–375.

Roberts, J. E. & DeSouza, J. M. 1958. The compressibility of sands. *Proc. Am. Soc. Test. Mater.* **58**, 1269–1277.

Rochon, R. W. 1967. Relationship of mineral composition of shales to density. *Trans. Gulf Coast Ass. geol. Soc.* **17**, 135–142.

Sawabini, C. T., Chilingarian, G. V. & Allen, D. R. 1974. Compressibility of unconsolidated arkosic oil sands. *Soc. Petrol. Engr. J.* **14**, 132–138.

Scarbrough, M. G. 1992. Numerical modelling of the Mexican Ridges Foldbelt, Gulf of Mexico. Ph.D. dissertation, Purdue Univ.

Scholle, P. A. (ed.). Geologic studies on the COST No. B-2 Well, U.S. Mid-Atlantic outer continental shelf area. U.S. Geol. Survey Circular 750.

Sclater, J. & Christie, P. A. F. 1980. Continental stretching: an explanation for the post-mid-Cretaceous subsidence of the central North Sea Basin. *J. geophys. Res.* **85**, 3711–3739.

Selley, R. C. 1978. Porosity gradients in North Sea oil-bearing sandstones. *J. geol. Soc. Lond.* **135**, 119–132.

Skempton, A. W. 1944. The consolidation of muddy sediments. *Q. J. geol. Soc. Lond.* **100**, 119–135.

Skempton, A. W. 1953. Soil mechanics in relation to geology. *Proc. Yorkshire geol. Soc.* **29**, 33–62.

Sowers, G. F. 1979. *Introductory Soil Mechanics and Foundations.* MacMillan, New York.

Stanton, G. D. 1977. Secondary porosity in sandstones of the Lower Wilcox (Eocene), Karnes County, Texas. *Trans. Gulf Coast Ass. geol. Soc.* **27**, 197–207.

Suter, M. 1987. Orientation data on the state of stress in northeastern Mexico as inferred from stress-induced borehole elongations. *J. geophys. Res.* **92**, 2617–2626.

Tada, R. & Siever, R. 1989. Pressure solution during diagenesis. *Annu. Rev. Earth & Planet Sci.* **17**, 89–118.

Tharp, T. M. 1985. Numerical models of subduction and forearc deformation. *Geophys. J. R. astr. Soc.* **80**, 419–437.

Tompkins, R. E. & Shepherd, L. E. 1979. Orca Basin: depositional processes, geotechnical properties and clay mineralogy of Holocene sediments within an anoxic hypersaline basin, Northwest Gulf of Mexico. *Marine Geotechnol.* **33**, 221–238.

Tschebotarioff, G. 1951. *Soil Mechanics, Foundations, and Earth Structures.* McGraw-Hill, New York.

Vaid, Y. P. 1985. Effect of consolidation history and stress path on hyperbolic stress-strain relations. *Can. J. Geotech.* **22**, 172–176.

van der Knaap, W. & van der Vlis, A. C. 1967. On the cause of subsidence in oil-producing areas. *Seventh Trans. World Petrol. Congr.* **3**, 85–95.

Westbrook, G. K. & Smith, M. J. 1983. Long decollements and mud volcanoes: evidence from the Barbados Ridge complex for the role of high pore-fluid pressure in the development of an accretionary complex. *Geology* **11**, 279–283.

Wolf, K. H. & Chilingarian, G. V. 1976. Diagenesis of sandstones and compaction. In: *Compaction of Coarse-Grained Sediments, II* (edited by Chilingarian, G. V. & Wolf, K. H.). Elsevier, New York. 69–444.

Wroth, C. P. & Houlsby, G. T. 1985. Soil mechanics—property characterization and analysis procedures. In: *Proc. Eleventh Int. Conf. Soil Mech. Found. Engr.* 1, Balkema, Rotterdam, 1–55.

Xiao, H.-B., Dahlen, F. A. & Suppe, J. 1991. Mechanics of extensional wedges. *J. geophys. Res.* **96**, 10301–10818.

Yong, R. K. & Ko, H.-Y. (eds) 1981. *Limit Equilibrium, Plasticity, and Generalized Stress–Strain in Geotechnical Engineering.* Am. Soc. Civil Engr. New York.

Zienkiewicz, O. C. 1971. *The Finite Element Method in Engineering Science.* 2nd edition. McGraw-Hill, London.